4D transverse phase space tomography of an operational hydrogen ion beam via noninvasive 2D measurements using laser wires

Jonathan C. Wong,* Andrei Shishlo, Alexander Aleksandrov, Yun Liu, and Cary Long
Oak Ridge National Laboratory, Oak Ridge, Tennessee 37831, USA

(Received 21 November 2021; accepted 23 March 2022; published 13 April 2022)

Utilizing noninvasive 2D scans with laser wires, we tomographically reconstructed the 4D transverse phase space distribution of a 1-GeV hydrogen ion (i.e., H^-) beam during operation. The 4D tomography is based on two new advances. First, we extended the formulation of maximum entropy phase space tomography to take 2D projections as input and derived theoretical results relevant to our application. Second, we introduced the method of "perpendicular scans" to obtain cross-plane information from a laser wire emittance scanner. Perpendicular scans are two unconventional 2D measurements performed with perpendicular front and back wires. In contrast, only parallel front and back wires (i.e., "parallel scans") are utilized in ordinary measurements of the horizontal and vertical 2D phase space distributions. When we applied the technique to the laser emittance station in the high-energy beam transport of the Spallation Neutron Source, experimental results showed that perpendicular scans can provide significant new information to the reconstructed 4D phase space distribution.

DOI: 10.1103/PhysRevAccelBeams.25.042801

I. INTRODUCTION

A. Phase space tomography

Tomography is the reconstruction of a multidimensional distribution from its lower-dimensional projections. In the context of beam diagnostics, where the number of measured projections ≈ 10, tomographic reconstruction of the beam phase space distribution is typically an inverse problem with nonunique solutions. One commonly adopted approach in solving such an underdetermined problem is to invoke the principle of maximum entropy (MENT), which states that, among the many possible solutions, one should select the solution that maximizes the entropy of the resulting distribution. A general discussion of the MENT principle and its usage in data analysis can be found in Ref. [1].

MENT tomographic reconstruction for beam diagnostics was first formulated and applied at Los Alamos National Laboratory (LANL) [2,3]. In these pioneering studies, 2D and 4D transverse phase space distributions were reconstructed from wire scanner measurements of 1D beam density profiles. The technique of MENT tomography has since been widely employed in many accelerator facilities to characterize the beam phase space distribution, e.g., [4–8].

To help simplify the ensuing discussion, we introduce the terms "2D-from-1D beam tomography" and "4D-from-1D beam tomography" to denote the aforementioned 2D and 4D transverse phase space reconstruction from 1D beam profile measurements. Similarly, "4D-from-2D beam tomography" refers to the reconstruction of 4D transverse phase space from 2D projections.

While 2D-from-1D and 4D-from-1D beam tomography are common, few studies have been performed on 4D-from-2D beam tomography, because direct 2D phase space measurements are more complicated and less available than 1D profile measurements. Three previous studies on 4D-from-2D beam tomography are Refs. [9–11], and none employed the MENT principle in obtaining the solutions.

In this paper, we extend our work in Ref. [12] and present the first results on 4D-from-2D beam tomography using the MENT principle. With advances in both data collection (new cross-plane scans) and data analysis (theoretical results on MENT tomography), we successfully utilized the laser wire system [13,14] at the Spallation Neutron Source (SNS) [15] to take noninvasive 2D measurements and reconstruct the 4D transverse phase space distribution of a 1-GeV hydrogen ion (i.e., H^-) beam during operation.

B. Organization

The paper is organized as follows. Section II reviews MENT tomography and extends the formulation such that 2D projections can be taken as input for the purposes of 4D-from-2D beam tomography. The analytical solution of an important special case is proved, and the algorithm for

*wongchu1@msu.edu

numerical solution of the general case is presented. Section III describes the laser emittance station in the SNS high-energy beam transport (HEBT) and how it performs phase space measurements on a H^- beam. Section IV shows that, in addition to the two routine parallel scans, one can introduce two "perpendicular scans" which contain information on x-y coupling. With this new method, four noninvasive 2D measurements of the 4D transverse phase space distribution can be taken without changing the beam optics. A coordinate transformation is also introduced to cast this particular MENT tomography problem into a more elegant form. The symmetrical properties of the transformed problem is exploited in Sec. V to derive a rigorous error bound on the MENT solution. The derivation relies on the total variation distance, a measure that quantifies the difference between two phase space distributions. Detailed proofs of certain results in Sec. V are included in the Appendix A.

Using the tools developed in preceding sections, Sec. VI shows experimental results of 4D-from-2D beam tomography of an operational 1-GeV H^- beam in the SNS HEBT. We obtained two MENT solutions, one using only the two parallel scans and one using all four scans (two parallel and two perpendicular). Comparison between these two solutions shows that the two perpendicular scans provide valuable information and bring much richer structure to the 4D transverse phase space distribution. Tomography results also find finite x-y coupling in the 4D transverse phase space distribution. We employ a simulation example in Appendix B to verify that the MENT tomography technique we employed can obtain accurate information on x-y coupling. Finally, we conclude our findings and outline further work in Sec. VII.

II. MENT TOMOGRAPHIC RECONSTRUCTION

A. Formulation

We extend the formulation of MENT tomography such that 2D projections can be used as input data. The approach closely follows the pioneering work at LANL [2,3] which dealt with 1D projections.

To reconstruct a 4D transverse phase space distribution from 2D projections, the MENT approach seeks to maximize the entropy:

$$H[\rho] = -\iiiint \rho(x,x',y,y') \ln \rho(x,x',y,y') dx dx' dy dy' \quad (1)$$

given n constraint equations, with n being the number of 2D measurements. The jth constraint equation is given by

$$\begin{aligned} G_j[\rho] &= g_j(u_j,u_j') - \iint \rho[\vec{x}(\vec{u}_j)] dv_j dv_j' \\ &= g_j(u_j,u_j') - \iint \rho(\mathbf{A}_j^{-1}\vec{u}_j) dv_j dv_j' \\ &= 0, \end{aligned} \quad (2)$$

where $g_j(u_j,u_j')$ is a measured 2D projection. $\vec{u}_j$, the coordinates over which the jth projection is taken, and $\vec{x}$, the transverse phase space coordinates of the beam at the reconstruction location, are assumed to be related by a linear transformation:

$$\vec{u}_j \equiv \begin{pmatrix} u_j \\ v_j \\ u_j' \\ v_j' \end{pmatrix} = \mathbf{A}_j \begin{pmatrix} x \\ y \\ x' \\ y' \end{pmatrix} \equiv \mathbf{A}_j \vec{x} \quad (3)$$

with $\mathbf{A}_j$ being a 4×4 matrix.

The MENT solution can be found by introducing a new functional that contains Lagrange multiplier functions:

$$K[\rho] = H[\rho] + \sum_{j=1}^{n} \iint \lambda_j(u_j,u_j') G_j[\rho] dv_j dv_j'. \quad (4)$$

The variation of $K[\rho]$ by ρ should vanish, which leads to

$$\begin{aligned} \rho &= C_1 \exp\left(\sum_{j=1}^{n} \lambda_j(u_j,u_j') - 1\right) \\ &= C_2 \prod_{j=1}^{n} h_j(u_j,u_j') \end{aligned} \quad (5)$$

with C_1 and C_2 being constants. Hence, the MENT solution is a product of n component functions h_j which are to be solved using the constraint equations. We present the analytical solution for a special case in Sec. II B, followed by Sec. II C which discusses how to obtain a numerical solution in the general case.

B. Two-scan analytical solution

Two 2D projections of the 4D transverse phase space are routinely measured: the horizontal and vertical 2D phase space distributions $\rho_{xx'}(x,x')$ and $\rho_{yy'}(y,y')$. Given only these two 2D projections, the constraint equations expressed in the form of Eq. (2) are

$$\begin{aligned} G_1[\rho] &= \rho_{xx'}^{(\mathrm{meas})}(x,x') - \iint \rho(x,x',y,y')\, dy dy' \\ &= 0, \end{aligned} \quad (6)$$

$$\begin{aligned} G_2[\rho] &= \rho_{yy'}^{(\mathrm{meas})}(y,y') - \iint \rho(x,x',y,y')\, dx dx' \\ &= 0. \end{aligned} \quad (7)$$

It can then be seen from Eq. (5) that the MENT solution to ρ has the form

$$\rho(x,x',y,y') = f_1(x,x') f_2(y,y'). \quad (8)$$

We can plug Eq. (8) into Eq. (6) and invoke normalization to get

$$f_1(x,x') = \rho_{xx'}^{(\mathrm{meas})}(x,x') \tag{9}$$

and similarly for $f_2(y,y')$.

Therefore, given only the horizontal and vertical 2D phase space measurements, MENT tomographic reconstruction has the analytical solution

$$\rho(x,x',y,y') = \rho_{xx'}^{(\mathrm{meas})}(x,x')\rho_{yy'}^{(\mathrm{meas})}(y,y'). \tag{10}$$

Such a phase space distribution has no x-y coupling at all, which seems to be a natural consequence of the fact that the input data provide no cross-plane information.

A consequence of Eq. (10) is that any cross-plane 2D projection is simply the product of the respective 1D distributions; for example

$$\begin{aligned}\rho_{xy}(x,y) &= \iint \rho(x,x',y,y')dx'dy' \\ &= \int \rho_{xx'}^{(\mathrm{meas})}(x,x')dx' \int \rho_{yy'}^{(\mathrm{meas})}(y,y')dy' \\ &= \rho_x^{(\mathrm{meas})}(x)\rho_y^{(\mathrm{meas})}(y).\end{aligned} \tag{11}$$

C. Numerical solution

In general, component functions of Eq. (5), and, hence, the MENT distribution, have to be solved numerically using the n constraint equations. Combining Eqs. (2) and (5), we obtain n coupled equations:

$$g_k(u_k,u_k') = h_k(u_k,u_k') \iint C_2 \prod_{j=1,j\neq k}^{n} h_j(u_j,u_j')dv_k dv_k' \tag{12}$$

whereupon the component functions $h_k(u_k,u_k')$ can be solved iteratively using a Gauss-Seidel–type algorithm as shown in Eq. (13) below:

$$h_k^{(m+1)}(u_k,u_k') = \frac{g_k(u_k,u_k')}{\tilde{g}_k^{(m+1)}(u_k,u_k')}, \tag{13}$$

where

$$\begin{aligned}&\tilde{g}_k^{(m+1)}(u_k,u_k') \\ &= \iint C_2 \prod_{j=1}^{k-1} h_j^{(m+1)}(u_j,u_j') \prod_{j=k+1}^{n} h_j^{(m)}(u_j,u_j')dv_k dv_k'.\end{aligned} \tag{14}$$

The superscript in parentheses denotes the iterative index for the component function, starting from $m = 1$. As shown in Eq. (14), each updated function is immediately employed in all subsequent calculations. Since this algorithm does not guarantee convergence, if the solution does not converge after some number of iterations, we can resort to direct fitting, which will, of course, be much slower.

III. PHASE SPACE MEASUREMENT USING LASER WIRE

A laser-based noninvasive method [14] is used to perform 2D measurements of the transverse phase space of 1-GeV hydrogen ion (H^-) beams in the SNS HEBT downstream of the superconducting linac. The schematic of such a laser emittance station is shown in Fig. 1. The measurement consists of three steps. In the first step, a narrow slice of the neutralized hydrogen (H^0) beam is created by a focused laser beam, i.e., a laser wire, through the photoneutralization of the ion beam. In the second step, the H^0 beam slice is separated from the ion beam path in a dipole magnet and propagates directly to the linac dump. In the last step, the divergence angle of the H^0 beam slice is obtained via wire scanner measurements of its transverse profiles after its propagation over ≈11.6 m. Since the H^0 beam preserves the angular distribution of the original ion beam, the measurement of the divergence of the H^0 beam slice leads to the determination of the ion beam divergence.

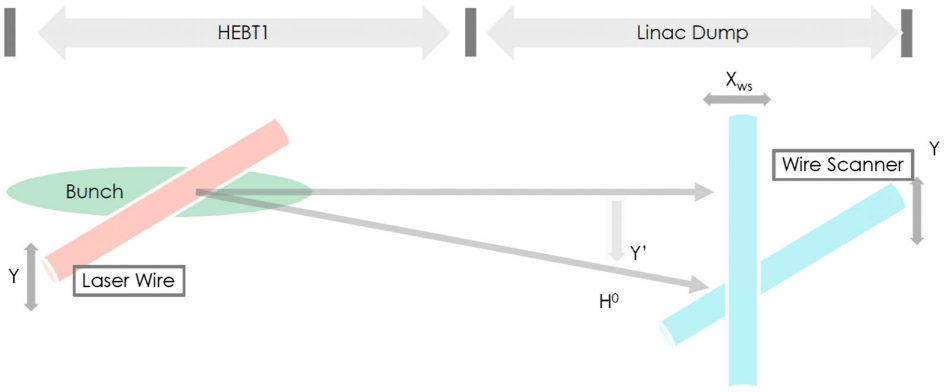

FIG. 1. Schematic of the laser wire station in the SNS HEBT.

By a nested scan of the laser and metal wires in horizontal or vertical directions, one takes a 2D measurement of the ion beam's transverse phase space distribution. As the photoneutralization results in only a negligible beam loss while the metal wire is located in the linac dump, the measurement process is completely noninvasive. Therefore, direct 2D measurements can be performed on a 1.4-MW neutron production ion beam which significantly improves the speed and accuracy.

The light source used in the measurements is a customized hybrid laser system including a fiber seeder and solid-state optical amplifiers [16]. The laser operates in a 30-Hz macropulse mode, and each macropulse consists of micropulses with a pulse width of ≈60 ps and a repetition rate of 402.5 MHz. Both macropulses and micropulses of the laser beam are synchronized to the ion beam. The recently upgraded laser system has a beam quality factor of about 1.2, and the focused laser beam diameter varies from 80 to 200 μm within an up to 10-mm laser-ion beam interaction region, which assures sufficient spatial resolution for the phase space measurement. Meanwhile, the metal wire used in the divergence angle measurement is composed of ten 50-μm titanium wires, a configuration that enables both high transmission of electrons and high detection efficiency. Positions of laser and metal wires are controlled with step motors which have position accuracy of better than 0.1 mm. In a typical phase space measurement, both the laser and the metal wires take 0.5-mm steps which translate into spatial and angular resolutions of 0.5 mm and 0.043 mrad, respectively. Quantities associated with wire sizes and their position errors have little effect on the resolutions, because they are much smaller than the wire step sizes. During the scan, the detector output is averaged over 15 laser pulses to improve the measurement accuracy. A measurement involving ≈1500 points in the phase space takes about 30 min to complete.

IV. 4D PHASE SPACE TOMOGRAPHY WITH 2D LASER WIRE SCANS

The technique of 4D MENT tomography from 2D projections can be applied to 2D measurements obtained using the SNS laser wire station described in Sec. III. In the rest of the paper, we refer to the laser metal wires as "slits" for simplicity. Functionally, the station performs two-slit–type emittance scans where the laser wires function as the 1st slit that selects a slice of particles and physical wires downstream of a drift act as the 2nd slit to detect the spread of the slice.

A. Parallel scans

When the two slits are parallel, such a configuration performs the usual emittance scans whose results are the 2D phase space distributions in the horizontal and vertical planes:

$$\iint \rho(x_i, x_i', y_i, y_i')\, dy_i dy_i' = \rho^{(\mathrm{meas})}_{x_i x_i'}(x_i, x_i'), \tag{15}$$

$$\iint \rho(x_i, x_i', y_i, y_i') dx_i dx_i' = \rho^{(\mathrm{meas})}_{y_i y_i'}(y_i, y_i'). \tag{16}$$

Here, we introduce a distinction between raw and processed data that will prove useful below. When we perform parallel scans, the actual raw data are distributions in two position coordinates (i.e., the position of the two wires) which we denote by $\tilde{\rho}^{(\mathrm{meas})}_{x_i x_f}(x_i, x_f)$ and $\tilde{\rho}^{(\mathrm{meas})}_{y_i y_f}(y_i, y_f)$. The 2D phase space distributions we want, $\rho^{(\mathrm{meas})}_{x_i x_i'}(x_i, x_i')$ and $\rho^{(\mathrm{meas})}_{y_i y_i'}(y_i, y_i')$, are derived from them by calculating angles based on the positions of the two wires. The conversion can be stated explicitly as follows:

$$\rho^{(\mathrm{meas})}_{x_i x_i'}\left(x_i, \frac{x_f - x_i}{L}\right) = L\tilde{\rho}^{(\mathrm{meas})}_{x_i x_f}(x_i, x_f), \tag{17}$$

$$\rho^{(\mathrm{meas})}_{y_i y_i'}\left(y_i, \frac{y_f - y_i}{L}\right) = L\tilde{\rho}^{(\mathrm{meas})}_{y_i y_f}(y_i, y_f), \tag{18}$$

where the subscripts i and f denote the longitudinal locations of the laser wire and physical wire, respectively. $L = 11.6$ m is the drift length between these two locations.

We must emphasize that we use the symbol $\tilde{\rho}_{u_j u_k}$ to denote 2D "position density functions" whose arguments are both positions, whereas the symbol $\rho_{v_j v_k'}$ represents 2D phase space distribution functions whose arguments contain one position and one angle. They even have different units as can be seen from Eqs. (17) and (18). Without going into any detail, we know the units must be balanced by inserting L to the appropriate power, because L is the only relevant length parameter in the setup.

Parallel scans do not contain any information on the dependence between horizontal and vertical phase space coordinates. If we perform only these two scans, the MENT solution would say there is no dependence as shown in Eq. (10).

B. Perpendicular scans

To obtain cross-plane information, two additional scans can be made with perpendicular slits where the laser wire was horizontal but the physical wire was vertical, or vice versa. Using the notation introduced above, these measurements correspond to the following 2D projections:

$$\iint \rho\left(x_i, \frac{x_f - x_i}{L}, y_i, y_i'\right) dx_i dy_i' = L\tilde{\rho}^{(\mathrm{meas})}_{x_f y_i}(x_f, y_i), \tag{19}$$

$$\iint \rho\left(x_i, x_i', y_i, \frac{y_f - y_i}{L}\right) dx_i' dy_i = L\tilde{\rho}^{(\mathrm{meas})}_{x_i y_f}(x_i, y_f). \tag{20}$$

To see Eq. (19), note that, when only the second wire is vertical (moved horizontally), the wire signal has contribution from all pairs of (x_i, x_i') that will arrive at x_f. Hence, the integrand has the form as shown, and an analogous reasoning applies to Eq. (20).

As discussed in Sec. IV A, scan results with perpendicular slits are not distributions in phase space coordinates. Therefore, they are denoted by $\tilde{\rho}_{u_j u_k}$ on the right-hand sides of Eqs. (19) and (20).

C. Coordinate transformation

While Eqs. (15), (16), (19), and (20) constitute a valid set of 2D projections for performing 4D-from-2D beam tomography, the perpendicular scans are not direct projections of the 4D phase space which render the solution more involved. The problem can be vastly simplified by introducing a coordinate transformation as follows.

Define a new set of coordinates x_i, x_f, y_i, y_f where

$$\begin{pmatrix} x_i \\ x_f \\ y_i \\ y_f \end{pmatrix} = \begin{pmatrix} 1 & 0 & 0 & 0 \\ 1 & L & 0 & 0 \\ 0 & 0 & 1 & 0 \\ 0 & 0 & 1 & L \end{pmatrix} \begin{pmatrix} x_i \\ x_i' \\ y_i \\ y_i' \end{pmatrix}. \tag{21}$$

The 4D beam distribution in this set of new coordinates is denoted by $\tilde{\rho}$:

$$\tilde{\rho}(x_i, x_f, y_i, y_f) = L^{-2}\rho\left(x_i, \frac{x_f - x_i}{L}, y_i, \frac{y_f - y_i}{L}\right). \tag{22}$$

The choice of symbol $\tilde{\rho}$, which is identical to that used for actual scan data in Secs. IV A and IV B, is no accident. With the given coordinate transformation, four orthogonal 2D projections of $\tilde{\rho}$, the beam distribution in transformed coordinates, are now measured directly by the parallel and perpendicular laser wire scans:

$$\iint \tilde{\rho}(x_i, x_f, y_i, y_f)dy_i dy_f = \tilde{\rho}^{(\mathrm{meas})}_{x_i x_f}(x_i, x_f), \tag{23}$$

$$\iint \tilde{\rho}(x_i, x_f, y_i, y_f)dx_i dx_f = \tilde{\rho}^{(\mathrm{meas})}_{y_i y_f}(y_i, y_f), \tag{24}$$

$$\iint \tilde{\rho}(x_i, x_f, y_i, y_f)dx_f dy_i = \tilde{\rho}^{(\mathrm{meas})}_{x_i y_f}(x_i, y_f), \tag{25}$$

$$\iint \tilde{\rho}(x_i, x_f, y_i, y_f)dx_i dy_f = \tilde{\rho}^{(\mathrm{meas})}_{x_f y_i}(x_f, y_i). \tag{26}$$

Such orthogonal projections are highly favorable to calculations. When one applies the MENT formalism for tomographic reconstruction, the linear transformation described by Eq. (3) is simply a permutation matrix for every constraint.

Furthermore, the set of 2D orthogonal projections in Eqs. (23)–(26) are highly symmetrical. If we take

$$\begin{pmatrix} x_1 \\ x_2 \\ x_3 \\ x_4 \end{pmatrix} = \begin{pmatrix} x_i \\ x_f \\ y_f \\ y_i \end{pmatrix}, \tag{27}$$

where the order of y_i and y_f is flipped, Eqs. (23)–(26) can be rewritten into the form

$$\iint \tilde{\rho}(x_1, x_2, x_3, x_4)dx_3 dx_4 = \tilde{\rho}^{(\mathrm{meas})}_{x_1 x_2}(x_1, x_2), \tag{28}$$

$$\iint \tilde{\rho}(x_1, x_2, x_3, x_4)dx_1 dx_2 = \tilde{\rho}^{(\mathrm{meas})}_{x_3 x_4}(x_3, x_4), \tag{29}$$

$$\iint \tilde{\rho}(x_1, x_2, x_3, x_4)dx_2 dx_4 = \tilde{\rho}^{(\mathrm{meas})}_{x_1 x_3}(x_1, x_3), \tag{30}$$

$$\iint \tilde{\rho}(x_1, x_2, x_3, x_4)dx_1 dx_3 = \tilde{\rho}^{(\mathrm{meas})}_{x_2 x_4}(x_2, x_4). \tag{31}$$

Equations (28)–(31) make explicit the symmetry of the constraint equations and the fact that every coordinate is included in two of the four 2D projections. These properties will be exploited to study error bounds in the section below.

V. INCONSISTENCIES IN MEASURED PROJECTIONS

When one performs MENT tomographic phase space reconstruction, the measured projections are invariably inconsistent among themselves. A few common reasons include (i) measurement errors, (ii) imperfect knowledge of the beam optics, and (iii) changing beam conditions throughout the course of measurements.

As a consequence, the MENT solution cannot possibly reproduce all measured projections perfectly; i.e., projections of the MENT solution must deviate from measured projections. A natural question then arises: How large are such deviations given the inconsistencies among measured projections?

To the best of our knowledge, no answer exists, in general, except for the qualitative argument that the deviations are small as long as the inconsistencies are minor. The fact that they are small is checked by comparing measured projections against projections from the MENT solution.

In this particular case, given the symmetrical structure of the 2D projections as given by Eqs. (28)–(31), we show that we can derive a simple expression that quantifies how inconsistencies in the measured projections impose a lower bound on the errors of the MENT solution.

A. Total variation distance

To explore how inconsistencies in the projections affect the MENT solution, we have to first define a measure that quantifies the difference between two distributions. The measure we have chosen is the total variation distance, which is defined as follows in 1D and 2D, respectively:

$$D_{\mathrm{TV}}[f(x), g(x)] \equiv \frac{1}{2}\int |f(x) - g(x)|dx, \tag{32}$$

$$D_{\mathrm{TV}}[f(x_1, x_2), g(x_1, x_2)] \equiv \frac{1}{2}\iint |f(x_1, x_2) - g(x_1, x_2)|dx_1 dx_2. \tag{33}$$

Although the same symbol D is used for the total variation distance of both 1D distributions and 2D distributions, one can readily distinguish between them by inspecting the dimension of the argument of the functional.

We note that, for normalized distributions, the total variation distance is 0 when the two distributions are identical and 1 if the two distributions are completely disjoint.

B. Error bound

We introduce the following notation to denote measured and reconstructed distributions. Measured 2D projections are denoted by $\rho^{(\mathrm{meas})}_{x_j x_k}(x_j, x_k)$. For each measured 2D projection, it is possible to obtain 1D projections via integration which are denoted by

$$\rho^{(\mathrm{meas},x_j x_k)}_{x_j}(x_j) \equiv \int \rho^{(\mathrm{meas})}_{x_j x_k}(x_j, x_k)dx_k, \tag{34}$$

$$\rho^{(\mathrm{meas},x_j x_k)}_{x_k}(x_k) \equiv \int \rho^{(\mathrm{meas})}_{x_j x_k}(x_j, x_k)dx_j. \tag{35}$$

In each case, the superscript "(meas)" indicates that the distribution comes from measurement. On the other hand, once 4D-from-2D beam tomography is performed, the solution to the phase space reconstruction is a 4D distribution whose projections can be obtained. Such projections are denoted by $\rho^{(\mathrm{sol})}_{x_j x_k}(x_j, x_k)$, where the superscript "(sol)" indicates that the distribution comes from the MENT solution.

In the context of 4D-from-2D beam tomography with laser wire scans, from four 2D scans, each 1D profile is effectively measured twice, and the two resulting distributions are not entirely consistent. An example of such inconsistencies is illustrated in Fig. 3.

Define

$$\mathfrak{D}(x_j; x_k, x_l) \equiv D_{\mathrm{TV}}[\rho^{(\mathrm{meas},x_j x_k)}_{x_j}(x_j), \rho^{(\mathrm{meas},x_j x_l)}_{x_j}(x_j)]. \tag{36}$$

Using the concept developed in Sec. V A, the degree of inconsistency between different projections can be quantified using the total variation distance. The fact that the measurements are inconsistent among themselves means every term on the right-hand side of

$$d_1 = \mathfrak{D}(x_1; x_2, x_3) + \mathfrak{D}(x_2; x_1, x_4) + \mathfrak{D}(x_3; x_1, x_4) + \mathfrak{D}(x_4; x_2, x_3) \tag{37}$$

is positive. Therefore,

$$d_1 > 0, \tag{38}$$

and we take d_1 to be a quantity that measures the overall degree of inconsistency among measured 2D projections.

After we perform 4D-from-2D beam tomography, 2D projections can be obtained from the solution and compared against measured 2D projections. Define the predicate

$$P(x_j, x_k)\colon\ \rho^{(\mathrm{sol})}_{x_j x_k}(x_j, x_k) \neq \rho^{(\mathrm{meas})}_{x_j x_k}(x_j, x_k). \tag{39}$$

Since the measured projections are themselves inconsistent, at least one of the measured projections must deviate from its counterpart obtained from the solution, i.e.:

$$P(x_1, x_2) \vee P(x_3, x_4) \vee P(x_1, x_3) \vee P(x_2, x_4) \text{ is true.} \tag{40}$$

Introducing the following notation for the 2D total variational distance of our interest:

$$\mathcal{D}(x_j, x_k) \equiv D_{\mathrm{TV}}[\rho^{(\mathrm{sol})}_{x_j x_k}(x_j, x_k), \rho^{(\mathrm{meas})}_{x_j x_k}(x_j, x_k)], \tag{41}$$

we know from Sec. V A that

$$P(x_j, x_k) \Rightarrow \mathcal{D}(x_j, x_k) > 0. \tag{42}$$

If we define a quantity d_2 as follows:

$$d_2 = \mathcal{D}(x_1, x_2) + \mathcal{D}(x_3, x_4) + \mathcal{D}(x_1, x_3) + \mathcal{D}(x_2, x_4), \tag{43}$$

Eqs. (40) and (42) imply

$$d_2 > 0. \tag{44}$$

In the language of MENT tomography, d_2 measures how far the MENT solution deviates from constraints which the solution should obey, whereas d_1 measures the inconsistency among the constraints themselves. We prove in Appendix A that

$$d_2 \geq \frac{1}{2} d_1. \tag{45}$$

This expression gives a rigorous lower bound on how well the MENT solution can agree with measured 2D projections. To our knowledge, such an error bound is the first known result of its kind.

VI. EXPERIMENTAL RESULTS IN SNS HEBT

Using the method of perpendicular scans described in Sec. IV, four 2D laser wire scans (two parallel and two perpendicular) were conducted on a 1-GeV hydrogen ion beam in the SNS HEBT. Taken while the beam was operational, these measurements were noninvasive and did not affect the ongoing neutron production.

All four 2D scan results are shown in the left column in Fig. 2. The two on the top are parallel scans which give the 2D phase space distribution in each respective plane, and the two on the bottom are perpendicular scans. Together, they constitute four 2D projections of the distribution $\tilde{\rho}(x_i, x_f, y_i, y_f)$ as described by Eqs. (15)–(20). Once $\tilde{\rho}(x_i, x_f, y_i, y_f)$ is tomographically reconstructed, it can be converted into the 4D transverse phase space distribution $\rho(x_i, x_i', y_i, y_i')$ using Eq. (22), or vice versa. For this reason, we will refer to $\tilde{\rho}$ and ρ interchangeably in the rest of this section.

A. Two-scan and four-scan MENT solutions

It is illuminating to consider two MENT solutions to this 4D-from-2D tomography problem. The respective 2D projections of both solutions are plotted in Fig. 2.

If we ignore the two perpendicular scans and consider only the two parallel scans which are routinely performed, MENT tomographic reconstruction has an analytical solution as given by Eq. (10). We refer to this as the two-scan solution and denote it by "sol 1." Being the product of the two measured 2D phase space distributions, the solution is exact in the sense that it must reproduce the input data perfectly. This can be seen by comparing the top two rows of the left and middle columns in Fig. 2.

If we use all four 2D projections, the 4D MENT solution can be obtained numerically using the iterative algorithm described in Sec. II C. After the MENT tomography problem is cast into the symmetrical form in Sec. IV C, the numerical solution typically converges within a few iterations. We refer to this as the four-scan solution and denote it by "sol 2." As we discussed in Sec. V, the four-scan MENT solution cannot perfectly reproduce the four 2D measured projections, because the measurement themselves are slightly inconsistent. Whether the four-scan solution is correct is investigated in detail in the following subsection.

B. Correctness of the four-scan solution

The inconsistencies among the four 2D scan results are shown in Fig. 3, where the 1D profile as measured by two projections are compared. The total variation distances between two measurements of each 1D profile are listed in Table I.

Such inconsistencies seem to have a minor effect on the four-scan solution if we compare the left and right columns in Fig. 2. Projections of the four-scan solution (right column) closely reproduce all four 2D measured projections (left column); this indicates that the numerical solution is valid.

To perform a more rigorous analysis enabled by theoretical results in Sec. V, we calculate the total variation distance between each of the measured 2D projection and its counterpart from the four-scan 4D MENT solution. The values are given in Table II.

Summing the total variation distances in Tables I and II, respectively, and using the notation from Sec. V, we find

$$d_1 = 0.2094, \tag{46}$$

$$d_2 = 0.1258. \tag{47}$$

Not only do the values of d_1 and d_2 satisfy the error bound condition in Eq. (45), d_2 is only slightly larger than the minimum value $d_1/2$. This means that the four-scan solution has reproduced the measured 2D projections almost as closely as is possible given the inconsistencies in the measurement data. In this sense, our analysis strongly suggests that the four-scan solution is correct.

C. Cross-plane information

The aim of this beam tomography experiment is to obtain detailed information on the 4D transverse phase space distribution with an emphasis on cross-plane information.

The inadequacy of the two-scan solution is immediately apparent from measurement results. As the discussion in Sec. II B shows, with parallel scans alone, the pair of coordinates x_i-y_f are independent of each other. As can be seen in the two bottom rows in Fig. 2, the two-scan solution would predict a star-shaped distribution for the 2D projection in x_i-y_f which strongly deviates from the distribution that was actually measured by the perpendicular scan. A similar phenomenon holds for the pair of coordinates y_i-x_f.

To answer whether perpendicular scans provide useful cross-plane information, we compare the two-scan solution against the four-scan solution below.

The four-scan solution can be illustrated by projecting the reconstructed distribution onto the four pairs of cross-plane coordinates whose 2D phase space distributions are not directly measured by the laser wire station. These results are shown in the middle left column in Fig. 4.

We also plot in the leftmost column in Fig. 4 the 2D phase space distributions of the two-scan solution (i.e., only the conventional parallel scans are used). One can observe that cross-plane projections of the two-scan solution display starlike or ellipselike shapes for reasons we already discussed above. These projections have much simpler structure than their counterparts from the four-scan solution.

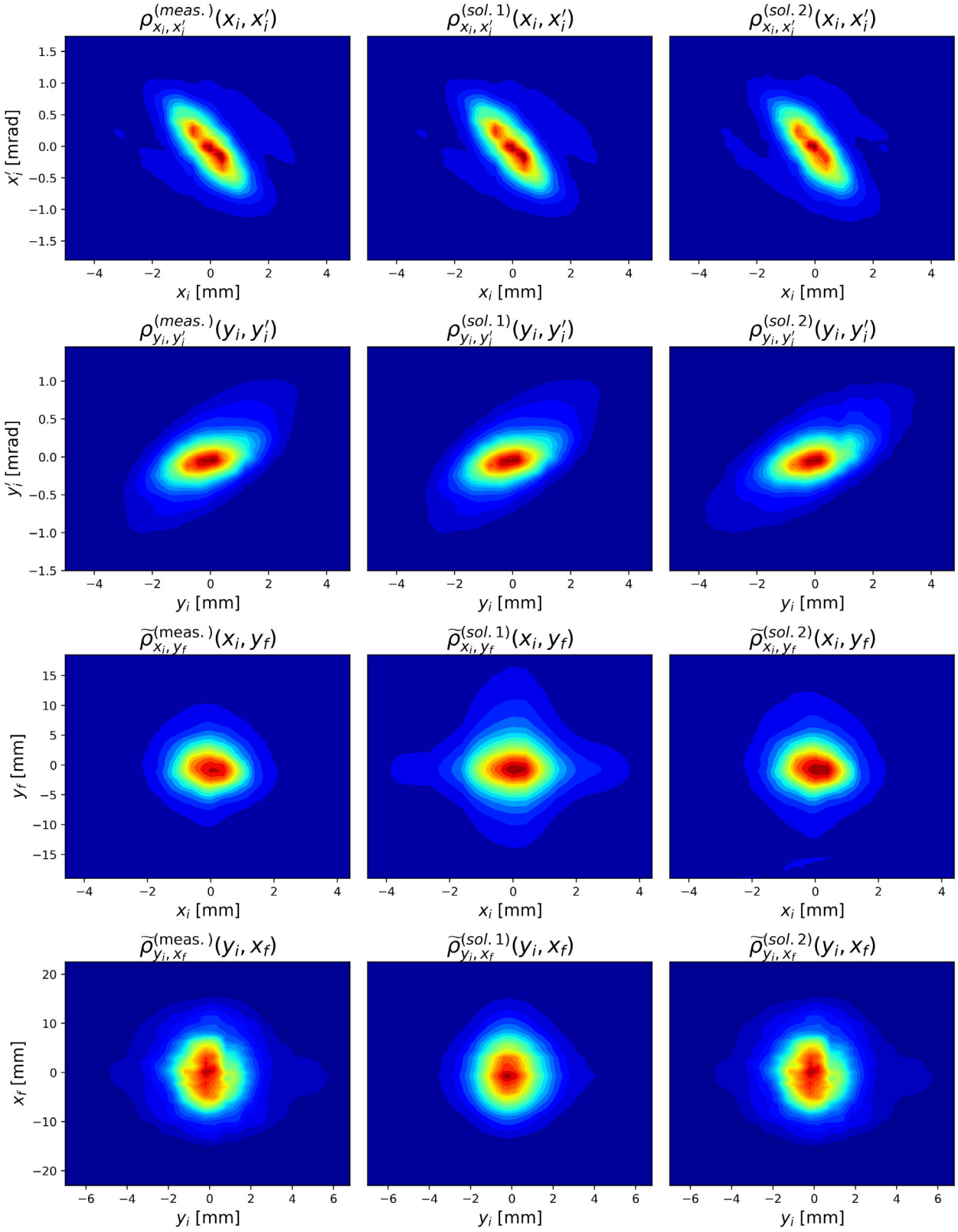

FIG. 2. Four 2D scan results at the SNS HEBT laser wire station (left column, denoted by superscript "meas") compared against the corresponding 2D projections of two 4D distributions (middle and right columns) that are tomographically reconstructed based on these scan results. Among the two reconstructed 4D distributions, the superscript "sol 1" denotes the two-scan analytical MENT solution that only uses the two conventional scans with parallel wires, whereas "sol 2" denotes the four-scan numerical MENT solution obtained using all four 2D scans.

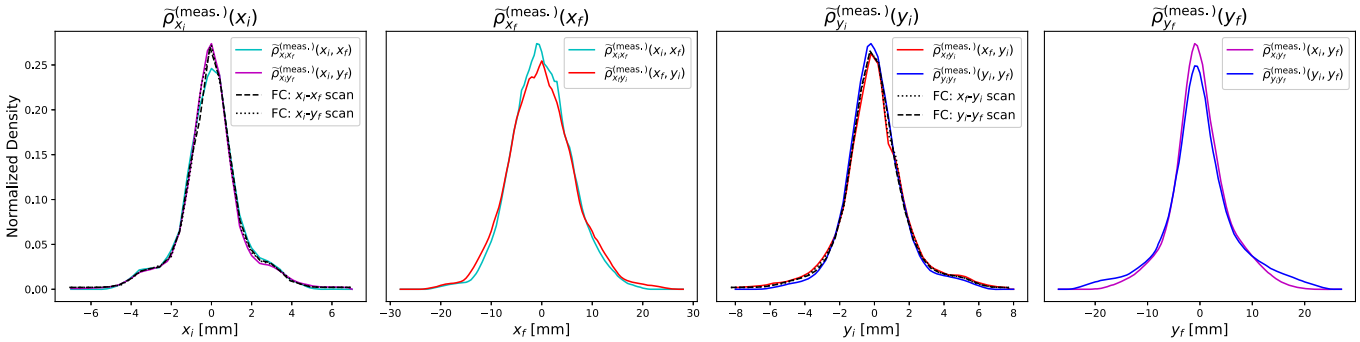

FIG. 3. Measured 1D profiles in the set of coordinates x_i, x_f, y_i, and y_f. The 1D profiles in solid lines are obtained from projections over the four 2D scan results at the SNS HEBT laser wire station. Each 1D profile can be obtained from two 2D scans, and both are plotted to illustrate their differences. The total variation distances between two different measurements of each 1D profile are shown in Table I. For x_i and y_i, the 1D profiles can also be measured separately by a Faraday cup which collected electrons stripped by the laser wire during the scan. These profiles, plotted in dashed and dotted lines, are consistent with projected 1D profiles from 2D scans and successfully verified their accuracy.

To further illustrate how the four-scan solution contains a much higher level of detail than the two-scan solution, we plot in the two columns on the right the normalized density of 1D slices of the 2D distributions of the four-scan solution. These 1D slice densities vary strongly with the value at which they are taken. This means that every pair of cross-plane coordinates is highly dependent. For example,

$$\rho^{(\mathrm{sol}\,2)}_{x_i y_i} \neq f_1(x_i) f_2(y_i) \tag{48}$$

and is far from any function of the form on the right-hand side.

In contrast, due to the independence between cross-plane coordinates [see Eq. (11)], each 1D slice density of the two-scan MENT solution always equals the 1D projected beam profile regardless of the location. The 1D projections of the two-scan MENT solution are denoted by black dotted lines. These results show that the 4D transverse phase space distribution has a much more sophisticated structure when perpendicular scans are included as input data.

We can also examine the second-order moments of the four-scan MENT solution—they are listed in Table III. The six uncoupled moments are all within 10% of the laser wire scan results, which again indicate that the MENT solution is valid. Furthermore, even though none of the four coupled moments are measured directly, they can be obtained from the reconstructed 4D transverse phase space distribution. Note that, if we do not take perpendicular scans, the two-scan MENT solution will predict that all four coupled moments are zero. The x–y coupling coefficients can be calculated as follows:

$$\frac{\langle x_i y_i \rangle}{\sqrt{\langle x_i x_i \rangle \langle y_i y_i \rangle}} = 0.10, \tag{49}$$

$$\frac{\langle x_i' y_i \rangle}{\sqrt{\langle x_i' x_i' \rangle \langle y_i y_i \rangle}} = 0.00, \tag{50}$$

$$\frac{\langle x_i y_i' \rangle}{\sqrt{\langle x_i x_i \rangle \langle y_i' y_i' \rangle}} = 0.12, \tag{51}$$

$$\frac{\langle x_i' y_i' \rangle}{\sqrt{\langle x_i' x_i' \rangle \langle y_i' y_i' \rangle}} = -0.04. \tag{52}$$

These results show that there exists a small correlation between the two transverse planes. We have confidence in these x-y coupling coefficients, because a simulation example in Appendix B shows that the 4D tomography technique we employed at the SNS HEBT can approximately recover coupled beam moments.

TABLE I. Total variation distances of 1D projections in x_i, x_f, y_i, and y_f as shown in Fig. 3.

Total variation distance	Value
$\mathfrak{D}(x_i; x_f, y_f)$	0.0446
$\mathfrak{D}(x_f; x_i, y_i)$	0.0405
$\mathfrak{D}(y_i; x_f, y_f)$	0.0577
$\mathfrak{D}(y_f; x_i, y_i)$	0.0666

TABLE II. Total variation distances between 2D laser wire scan results and 2D projections of the four-scan 4D reconstructed transverse phase space distribution.

Total variation distance	Value
$\mathcal{D}(x_i, x_f)$	0.0303
$\mathcal{D}(y_i, y_f)$	0.0478
$\mathcal{D}(x_i, y_f)$	0.0405
$\mathcal{D}(y_i, x_f)$	0.0072

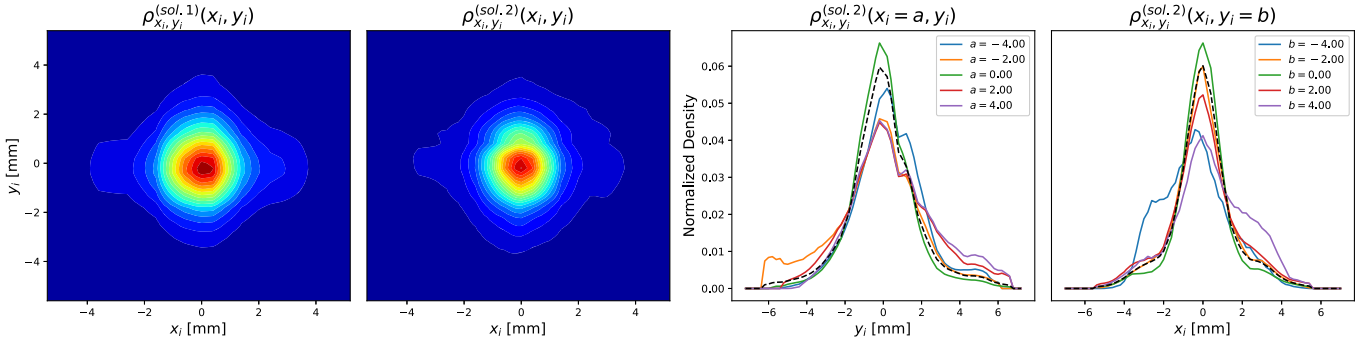

(a) x_i-y_i phase space

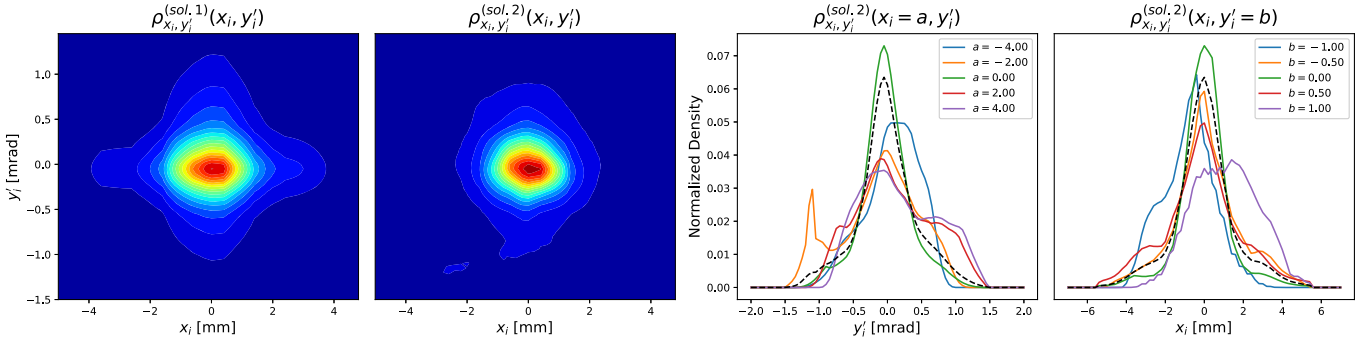

(b) x_i-y_i' phase space

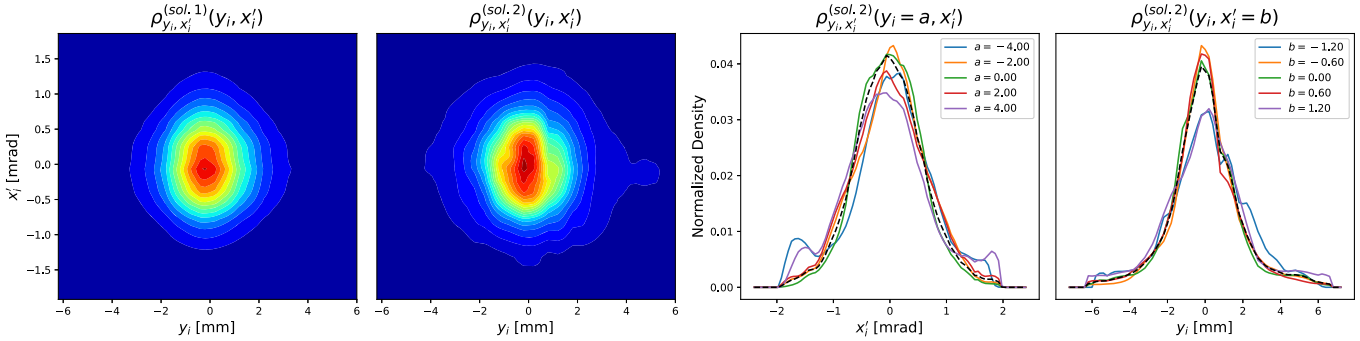

(c) y_i-x_i' phase space

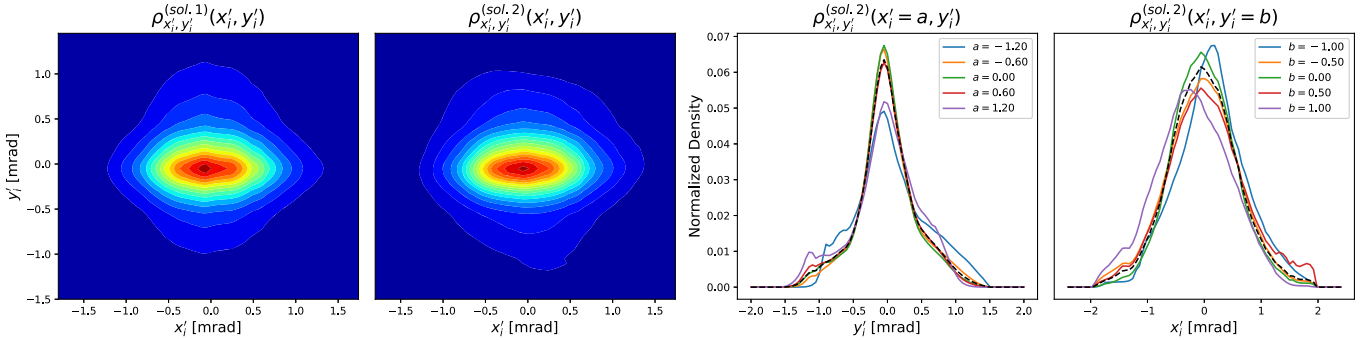

(d) x_i'-y_i' phase space

FIG. 4. Cross-plane 2D phase space projections of the 4D MENT numerical solution obtained from four 2D projections at the SNS HEBT laser wire station. The superscript sol 1 denotes the two-scan (parallel slits only) MENT solution, and sol 2 denotes the four-scan (both parallel and perpendicular slits) MENT solution.

TABLE III. Second-order moments of the beam's 4D transverse phase space distribution from (i) 2D laser wire scans and (ii) four-scan 4D MENT reconstruction.

Second-order beam moment	2D laser emittance scan	4D reconstructed distribution
$\langle x_i x_i \rangle$ [mm^2]	2.35	2.45
$\langle x_i x_i' \rangle$ [mm-mrad]	-5.10×10^{-1}	-5.33×10^{-1}
$\langle x_i' x_i' \rangle$ [mrad^2]	3.59×10^{-1}	3.87×10^{-1}
$\langle y_i y_i \rangle$ [mm^2]	3.37	3.50
$\langle y_i y_i' \rangle$ [mm-mrad]	5.18×10^{-1}	5.55×10^{-1}
$\langle y_i' y_i' \rangle$ [mrad^2]	1.82×10^{-1}	1.98×10^{-1}
$\langle x_i y_i \rangle$ [mm^2]	Not measured	2.85×10^{-1}
$\langle x_i' y_i \rangle$ [mm-mrad]	Not measured	2.27×10^{-3}
$\langle x_i y_i' \rangle$ [mm-mrad]	Not measured	8.31×10^{-2}
$\langle x_i' y_i' \rangle$ [mrad^2]	Not measured	-9.25×10^{-3}

VII. CONCLUSION

We extended the formulation of MENT tomography to reconstruct 4D transverse phase space distribution from multiple 2D projections. To perform such 4D tomography at the SNS HEBT laser wire station, we proposed the method of perpendicular scans where, in addition to conventional configurations with parallel slits, two-slit–type 2D scans are conducted with perpendicular slits to obtain cross-plane information. For this particular tomography problem, we also derived a rigorous error bound on the MENT solution that arises from inconsistencies in measurements.

Utilizing noninvasive laser wire scans, we conducted a tomography study on the 1-GeV beam at the SNS during operation. Experimental results showed that, in comparison with just the horizontal and vertical 2D phase space measurements, the addition of perpendicular scans provides valuable information on x-y coupling and gives a MENT distribution with more sophisticated structure. In future implementation, this technique may enable online 4D transverse phase space tomography to improve understanding of the beam dynamics and enhance control of the beam at the stripping foil and target. With favorable initial results from the simulation example in Appendix B, how well the MENT solution in 4D-from-2D beam tomography agrees with the true phase space distribution will be a subject of further investigation.

ACKNOWLEDGMENTS

We are grateful to Alexander Zhukov from Oak Ridge National Laboratory for suggesting the use of perpendicular scans as a source of cross-plane information. This research used resources of the Spallation Neutron Source, which is a DOE Office of Science User Facility. This manuscript has been authored by UT-Battelle, LLC, under Contract No. DE-AC05-00OR22725 with the U.S. Department of Energy (DOE). The U.S. government retains and the publisher, by accepting the article for publication, acknowledges that the U.S. government retains a nonexclusive, paid-up, irrevocable, worldwide license to publish or reproduce the published form of this manuscript, or allow others to do so, for U.S. government purposes. DOE will provide public access to these results of federally sponsored research in accordance with the DOE Public Access Plan [17].

APPENDIX A: PROOF OF EQ. (45)

We first introduce two lemmas.

Lemma A1.—Suppose there are two functions $f(x_1, x_2)$ and $g(x_1, x_2)$ whose integrals are denoted as follows:

$$f_1(x_1) \equiv \int f(x_1, x_2) dx_2, \tag{A1}$$

$$f_2(x_2) \equiv \int f(x_1, x_2) dx_1, \tag{A2}$$

$$g_1(x_1) \equiv \int g(x_1, x_2) dx_2, \tag{A3}$$

$$g_2(x_2) \equiv \int g(x_1, x_2) dx_1. \tag{A4}$$

Then

$$D_{\mathrm{TV}}[f(x_1,x_2), g(x_1,x_2)] \geq \frac{1}{2} D_{\mathrm{TV}}[f_1(x_1), g_1(x_1)] + \frac{1}{2} D_{\mathrm{TV}}[f_2(x_2), g_2(x_2)]. \tag{A5}$$

To prove Lemma A1, we first prove that

$$D_{\mathrm{TV}}[f(x_1, x_2), g(x_1, x_2)] \geq D_{\mathrm{TV}}[f_1(x_1), g_1(x_1)], \tag{A6}$$

$$\begin{aligned} & D_{\mathrm{TV}}[f_1(x_1), g_1(x_1)] \\ &= \frac{1}{2} \int |f_1(x_1) - g_1(x_1)| dx_1 \\ &= \frac{1}{2} \int \left| \int f(x_1, x_2) dx_2 - \int g(x_1, x_2) dx_2 \right| dx_1 \\ &= \frac{1}{2} \int \left| \int f(x_1, x_2) - g(x_1, x_2) dx_2 \right| dx_1 \\ &\leq \frac{1}{2} \iint |f(x_1, x_2) - g(x_1, x_2)| dx_2 dx_1 \\ &= D_{\mathrm{TV}}[f(x_1, x_2), g(x_1, x_2)]. \end{aligned} \tag{A7}$$

Similarly,

$$D_{\mathrm{TV}}[f(x_1, x_2), g(x_1, x_2)] \geq D_{\mathrm{TV}}[f_2(x_2), g_2(x_2)]. \tag{A8}$$

Thus, a combination of Eqs. (A6) and (A8) proves Lemma A1.

Lemma A2.—

$$D_{\mathrm{TV}}[f(x),h(x)]+D_{\mathrm{TV}}[g(x),h(x)]\geq D_{\mathrm{TV}}[f(x),g(x)]. \tag{A9}$$

One can invoke the triangle inequality to obtain

$$\begin{aligned}&|f(x)-h(x)|+|g(x)-h(x)|\\&\quad\geq|f(x)-h(x)+h(x)-g(x)|\\&\quad\geq|f(x)-g(x)|,\end{aligned} \tag{A10}$$

whereupon integration over x proves Lemma A2.

To use the two lemmas, we first define

$$\mathcal{C}(x_j;x_k)\equiv D_{\mathrm{TV}}[\rho_{x_j}^{(\mathrm{sol})}(x_j),\rho_{x_j}^{(\mathrm{meas},x_jx_k)}(x_j)], \tag{A11}$$

where $\rho_{x_j}^{(\mathrm{sol})}(x_j)$ is the 1D projection of the 4D reconstructed phase space along the coordinate x_j.

From Eq. (41), we invoke Lemma A1 to obtain

$$\mathcal{D}(x_j,x_k)\geq\frac{1}{2}\mathcal{C}(x_j;x_k)+\frac{1}{2}\mathcal{C}(x_k;x_j), \tag{A12}$$

which can be applied to Eq. (43) to get

$$\begin{aligned}2d_2\geq{}&\mathcal{C}(x_1;x_2)+\mathcal{C}(x_2;x_1)+\mathcal{C}(x_3;x_4)+\mathcal{C}(x_4;x_3)\\&+\mathcal{C}(x_1;x_3)+\mathcal{C}(x_3;x_1)+\mathcal{C}(x_2;x_4)+\mathcal{C}(x_4;x_2).\end{aligned} \tag{A13}$$

Next, we observe that

$$\mathcal{C}(x_j;x_k)+\mathcal{C}(x_j;x_l)\geq\mathfrak{D}(x_j;x_k,x_l), \tag{A14}$$

because

$$\begin{aligned}&D_{\mathrm{TV}}[\rho_{x_j}^{(\mathrm{sol})}(x_j),\rho_{x_j}^{(\mathrm{meas},x_jx_k)}(x_j)]\\&\quad+D_{\mathrm{TV}}[\rho_{x_j}^{(\mathrm{sol})}(x_j),\rho_{x_j}^{(\mathrm{meas},x_jx_l)}(x_j)]\\&\quad\geq D_{\mathrm{TV}}[\rho_{x_j}^{(\mathrm{meas},x_jx_k)}(x_j),\rho_{x_j}^{(\mathrm{meas},x_jx_l)}(x_j)]\end{aligned} \tag{A15}$$

by Lemma A2.

Applying Eq. (A14) to Eq. (A13), we pair terms whose first arguments are identical to get

$$\begin{aligned}2d_2\geq{}&[\mathcal{C}(x_1;x_2)+\mathcal{C}(x_1;x_3)]+[\mathcal{C}(x_2;x_1)+\mathcal{C}(x_2;x_4)]\\&+[\mathcal{C}(x_3;x_1)+\mathcal{C}(x_3;x_4)]+[\mathcal{C}(x_4;x_2)+\mathcal{C}(x_4;x_3)]\\\geq{}&\mathfrak{D}(x_1;x_2,x_3)+\mathfrak{D}(x_2;x_1,x_4)\\&+\mathfrak{D}(x_3;x_1,x_4)+\mathfrak{D}(x_4;x_2,x_3)\\={}&d_1,\end{aligned} \tag{A16}$$

which proves Eq. (45).

APPENDIX B: SIMULATION EXAMPLE: TRUNCATED GAUSSIAN DISTRIBUTION WITH LARGE x-y COUPLING

In this Appendix, we simulate a truncated Gaussian beam with large x-y coupling to show that the 4D tomography technique developed in Sec. IV is capable of recovering cross-plane information in the 4D transverse phase space.

Taking the setup of the laser emittance station in the SNS HEBT, we generate a beam whose 4D transverse phase space distribution is a 4σ-truncated Gaussian distribution given by

$$\rho^{(\mathrm{sim})}(\mathbf{x})=\begin{cases}\rho(\mathbf{x}), & \text{if } \rho(\mathbf{x})\geq e^{-4},\\ 0, & \text{otherwise,}\end{cases} \tag{B1}$$

where

$$\rho(\mathbf{x})=\exp\left(-\frac{1}{2}\mathbf{x}^{\mathrm{T}}\boldsymbol{\Sigma}_{\mathbf{x}}^{-1}\mathbf{x}\right) \tag{B2}$$

with

$$\mathbf{x}=\begin{pmatrix}x_i\\x_i'\\y_i\\y_i'\end{pmatrix}. \tag{B3}$$

Normalization of $\rho(\mathbf{x})$ and $\rho^{(\mathrm{sim})}(\mathbf{x})$ are omitted for convenience. $\boldsymbol{\Sigma}_{\mathbf{x}}$ is the 4×4 input covariance matrix of the full Gaussian distribution whose values were chosen to (i) provide x and y emittances and beam sizes similar to the real measured values and (ii) introduce significant $x-y$ coupling. After truncation, the simulated 4D transverse phase space distribution $\rho^{(\mathrm{sim})}(\mathbf{x})$ has second-order moments as shown in Table IV. The x-y coupling coefficients are listed below:

TABLE IV. Second-order moments of the beam's 4D transverse phase space distribution for (i) the simulated distribution and (ii) four-scan 4D MENT reconstruction.

Second-order beam moment	Simulated distribution	4D reconstructed distribution
$\langle x_ix_i\rangle$ [mm^2]	2.08	2.08
$\langle x_ix_i'\rangle$ [mm-mrad]	-4.17×10^{-1}	-4.17×10^{-1}
$\langle x_i'x_i'\rangle$ [mrad^2]	3.00×10^{-1}	3.00×10^{-1}
$\langle y_iy_i\rangle$ [mm^2]	2.90	2.90
$\langle y_iy_i'\rangle$ [mm-mrad]	4.15×10^{-1}	4.15×10^{-1}
$\langle y_i'y_i'\rangle$ [mrad^2]	1.50×10^{-1}	1.50×10^{-1}
$\langle x_iy_i\rangle$ [mm^2]	7.13×10^{-1}	8.31×10^{-1}
$\langle x_i'y_i\rangle$ [mm-mrad]	-3.22×10^{-1}	-3.32×10^{-1}
$\langle x_iy_i'\rangle$ [mm-mrad]	1.76×10^{-1}	1.66×10^{-1}
$\langle x_i'y_i'\rangle$ [mrad^2]	-5.94×10^{-2}	-6.67×10^{-2}

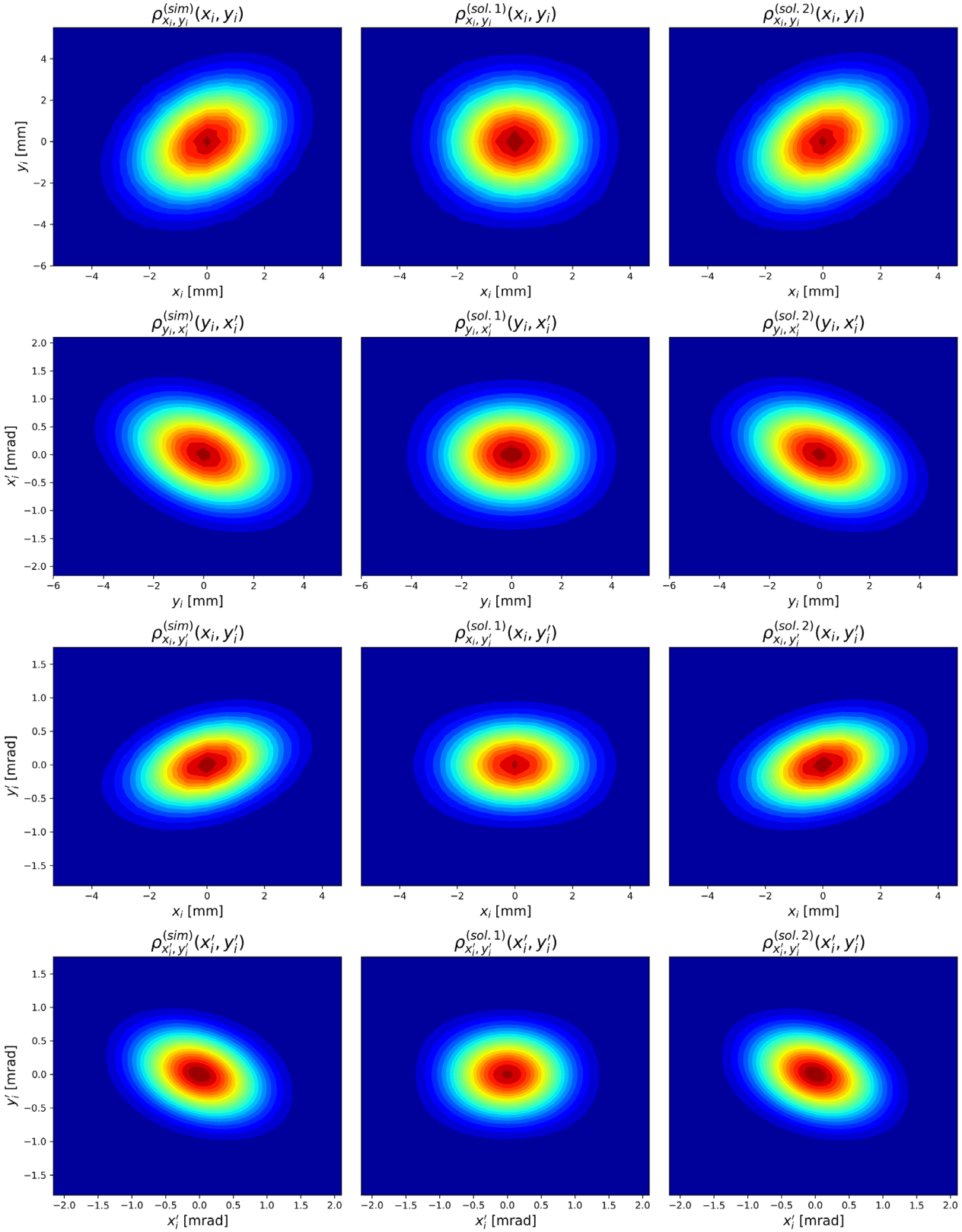

FIG. 5. Four cross-plane 2D projections of the transverse phase space distribution for (i) the simulated distribution (left column), (ii) the two-scan analytical solution (middle column), and (iii) the four-scan numerical solution (right column).

$$\frac{\langle x_i y_i \rangle}{\sqrt{\langle x_i x_i \rangle \langle y_i y_i \rangle}} = 0.29, \tag{B4}$$

$$\frac{\langle x_i' y_i \rangle}{\sqrt{\langle x_i' x_i' \rangle \langle y_i y_i \rangle}} = 0.32, \tag{B5}$$

$$\frac{\langle x_i y_i' \rangle}{\sqrt{\langle x_i x_i \rangle \langle y_i' y_i' \rangle}} = -0.35, \tag{B6}$$

$$\frac{\langle x_i' y_i' \rangle}{\sqrt{\langle x_i' x_i' \rangle \langle y_i' y_i' \rangle}} = -0.28, \tag{B7}$$

from which one can see that the coupling is strong.

In the simulation, four 2D scan results (two parallel scans and two perpendicular scans) are synthesized assuming the beam has transverse phase space distribution $\rho^{(\mathrm{sim})}(\mathbf{x})$ at the laser wire location. These four 2D scans are used to perform 4D MENT tomography on the transverse phase space distribution. Just as we did with the real measurement data in Sec. VI, both the two-scan analytical solution and four-scan numerical solutions are obtained. They are denoted by sol 1 and sol 2, respectively. The four-scan numerical solution is valid as it reproduced the synthesized measurement results perfectly—this is shown in Table IV where uncoupled second-order moments (i.e., the first six) of the four-scan solution are shown to be identical to those of the simulated distribution.

To examine whether the MENT solutions correctly reconstruct the simulated distribution which has large x-y coupling, we plot in Fig. 5 the four cross-plane 2D projections for the simulated distribution and the two 4D MENT solutions. As we expect based on the discussion in Sec. II B, if we take only the two conventional 2D phase space measurements in the horizontal and vertical planes (i.e., parallel scans), the MENT solution for the 4D transverse phase space contains no x-y coupling at all. On the other hand, if we also take perpendicular scans, comparisons between the left and right columns in Fig. 5 show that the four-scan MENT solution produces cross-plane projections that are close to the projections of the true distribution (the true distribution is the simulated distribution in this example). The second-order moments of the simulated distribution and the four-scan MENT solution are listed in Table IV. One can observe that, for the four coupled moments, the MENT solution is accurate to within ≈10%. These results, thus, verify that the 4D MENT tomography technique we developed can recover cross-plane information.

[1] D. S. Sivia and J. Skilling, *Data Analysis: A Bayesian Tutorial* (Oxford University, New York, 2012).

[2] G. N. Minerbo, O. R. Sander, and R. A. Jameson, Four-dimensional beam tomography, IEEE Trans. Nucl. Sci. **28**, 2231 (1981).

[3] C. T. Mottershead, Maximum entropy beam diagnostic tomography, IEEE Trans. Nucl. Sci. **32**, 1970 (1985).

[4] F. Löhl, S. Schreiber, M. Castellano, G. Di Pirro, L. Catani, A. Cianchi, and K. Honkavaara, Measurements of the transverse emittance at the FLASH injector at DESY, Phys. Rev. Accel. Beams **9**, 092802 (2006).

[5] D. Reggiani, C. K. Allen, and M. Seidel, Transverse phase-space beam tomography at PSI and SNS proton accelerators, in *Proceedings of the 1st International Particle Accelerator Conference (IPAC'10), Kyoto, Japan, 2010* (JACoW, Geneva, 2010), pp. 1128–1130.

[6] Y.-N. Rao and R. A. Baartman, Transverse phase space tomography in TRIUMF injection beamline, in *Proceedings of the 2nd International Particle Accelerator Conference (IPAC'11), San Sebastian, Spain, 2011* (JACoW, Geneva, 2011), pp. 1144–1146.

[7] K. Hock, M. Ibison, D. Holder, B. Muratori, A. Wolski, G. Kourkafas, and B. Shepherd, Beam tomography research at Daresbury laboratory, Nucl. Instrum. Methods Phys. Res., Sect. A **753**, 38 (2014).

[8] M. Scholz and B. Beutner, Electron beam phase space tomography at the European XFEL injector, in *Proceedings of the 8th International Particle Accelerator Conference (IPAC'17), Copenhagen, Denmark, 2017* (JACoW, Geneva, 2017), pp. 196–198.

[9] A. Friedman, D. P. Grote, C. M. Celata, and J. W. Staples, Use of projectional phase space data to infer a 4D particle distribution, Laser Part. Beams **21**, 17 (2003).

[10] K. Hock and A. Wolski, Tomographic reconstruction of the full 4D transverse phase space, Nucl. Instrum. Methods Phys. Res., Sect. A **726**, 8 (2013).

[11] M. Wang, Z. Wang, D. Wang, W. Liu, B. Wang, M. Wang, M. Qiu, X. Guan, X. Wang, W. Huang, and S. Zheng, Four-dimensional phase space measurement using multiple two-dimensional profiles, Nucl. Instrum. Methods Phys. Res., Sect. A **943**, 162438 (2019).

[12] C. Wong and A. Shishlo, Maximum entropy reconstruction of 4D transverse phase space from 2D projections: with application to laser wire measurements in the SNS HEBT, in *Proceedings of the 12th International Particle Accelerator Conference (IPAC'21), Campinas, Brazil, 2021* (JACoW, Geneva, 2021), pp. 1008–1011.

[13] Y. Liu, A. Aleksandrov, S. Assadi, W. Blokland, C. Deibele, W. Grice, C. Long, T. Pelaia, and A. Webster, Laser wire beam profile monitor in the Spallation Neutron Source (SNS) superconducting linac, Nucl. Instrum. Methods Phys. Res., Sect. A **612**, 241 (2010).

[14] Y. Liu, A. Aleksandrov, C. Long, A. Menshov, J. Pogge, A. Webster, and A. Zhukov, Nonintrusive emittance measurement of 1 GeV H^- beam, Nucl. Instrum. Methods Phys. Res., Sect. A **675**, 97 (2012).

[15] S. Henderson *et al.*, The Spallation Neutron Source accelerator system design, Nucl. Instrum. Methods Phys. Res., Sect. A **763**, 610 (2014).

[16] Y. Liu, C. Long, and A. Aleksandrov, Nonintrusive measurement of time-resolved emittances of 1-GeV operational hydrogen ion beam using a laser comb, Phys. Rev. Accel. Beams **23**, 102806 (2020).

[17] http://energy.gov/downloads/doe-public-access-plan.